Supplementary Information

Dynamic strength of iron under pressure-temperature conditions of Earth's inner core

Yong-Jae Kim[1,†,*], Gaia Righi[1,†], Orlando R Deluigi[2], Eduardo M Bringa[2], Thomas E Lockard[1],
Robert E Rudd[1], Carlos J Ruestes[3], Camelia V Stan[1], Christopher E Wehrenberg[1],
Arianna E Gleason[4,5], Marc A. Meyers[6], Hye-Sook Park[1]

[1]*Lawrence Livermore National Laboratory, Livermore, CA 94550, USA*
[2]*CONICET and Facultad de Ingeniería, Universidad de Mendoza, M5500 Mendoza, Argentina*
[3]*Instituto de Fusión Nuclear Guillermo Velarde and Departamento de Ingeniería Energética, ETSI de Industriales, Universidad Politécnica de Madrid, E-28006 Madrid, Spain*
[4]*Stanford University, Stanford, California 94305, USA*
[5]*SLAC National Accelerator Laboratory, Menlo Park, California 94025, USA*
[6]*University of California, San Diego, La Jolla, CA 92093, USA*

**Corresponding author. Email: kim100@llnl.gov*
†These authors contributed equally to this work.

Physics package layout

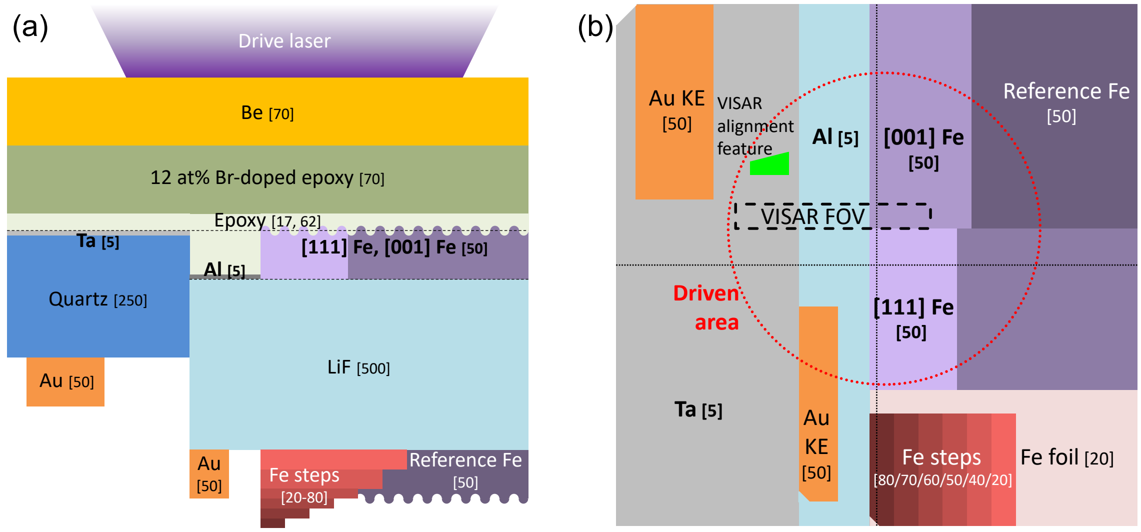

Figure S1. Sketches of the target physics package; (a) view from the side, and (b) plan view from the target chamber center.

Experimental configuration

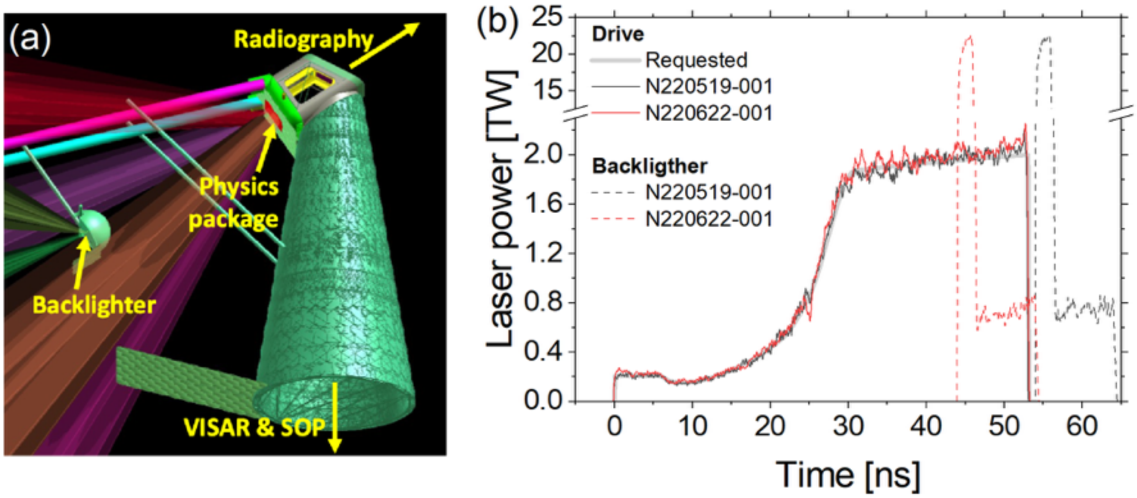

Figure S2. (a) A VisRad[1] image of the target, backlighter, and laser configuration. (b) Delivered laser powers of drive (solid) and backlighter (dashed) beams. Peak centers of backlighter beams are 55 ns for the N220519-001 shot (black) and 45 ns for the N220622-001 shot (red).

Velocity analysis

Reflections from the stationary free surfaces of the LiF and Quartz windows produce ghost fringes whose intensity is constant during the travel of the shock wave through the windows. After the ghost fringes are subtracted from the images[2,3] (Fig. S3a and b), standard phase unwrapping is performed to obtain apparent velocity (u_a) which is corrected to true velocity (u_t).

In the [001] Fe-LiF region, a shock wave breaks out of Fe at 23.1 ns and its intensity drops suddenly at 26.7 ns. We suspect the existence of an unwanted air gap (15 μm thick). The Fe free surface moves until it contacts the LiF (at 26.7 ns), so the measured apparent velocity is same as the true velocity; $u_t = u_a/n_{vac}$, where n_{vac}, is the refractive index of vacuum. The Fe-LiF interface is traced between 26.7 ns and 50.0 ns until the LiF becomes opaque, (at 50 ns) during which a relation by Kirsch[4] is used for a correction; $u_t = Au_a^B + Cu_a^D$ where $A = 0.7831$, $B = 0.9905$, $C = -1.866 \times 10^{-5}$, and $D = 3.681$. Then the shock wave exits from the LiF at 63.0 ns.

The unwanted air gap is also suspected between Al and LiF. The Al free surface starts to move when a shock wave reaches at 22.7 ns, until it contacts the LiF at 26.4 ns, traveling 24 μm. The Al-LiF interface is traced between 26.4 and 40.5 ns before the LiF becomes opaque, and the shock wave exists the LiF at 60.3 ns.

A shock wave breaks out of Ta at 19.0 ns and the Ta-Quartz interface moves until 29.3 ns. In this period, the correction is made with a zero-density refractive index of quartz ($n_0 = 1.0953$); $u_t = u_a/n_0$[5]. At 29.3 ns, fringe intensity drops suddenly, because a reverberating shock wave breaks out of the Ta and is strong enough to make the shock compressed quartz reflective. In this regime, and until it exits the Quartz at 44.2 ns, the apparent velocity is divided by the refractive index of quartz ($n_{Qtz} = 1.542$) for the correction; $u_t = u_a/n_{Qtz}$. The uncertainty of the phase retrieval is determined by the value which is needed to get the error bars of the velocity traces from the two VISAR channels to overlap, which is found as 3-5% of the VPF.

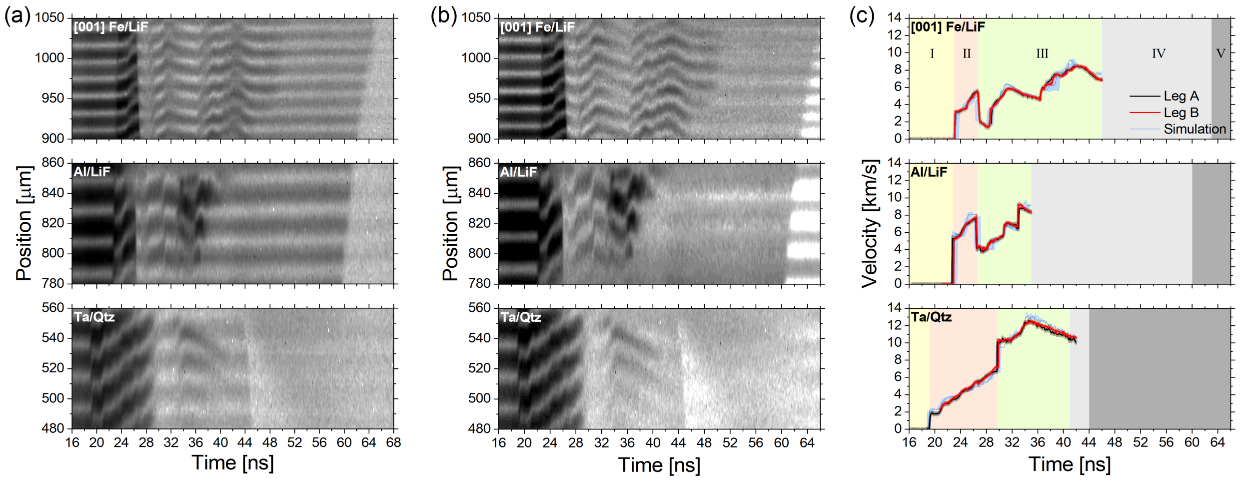

Figure S3. VISAR data from shot N220622 for [001] Fe, Al, and Ta (a) before and (b) after ghost fringe removal, and (c) their velocity traces with comparison to hydrodynamic simulations. Roman numbers in (c) represent different regions: I: an wave front has not yet reached the back surface of the sample (Fe, Al, and Ta) and the fringe data are obtained from the stationary back surface; II: the back surface begins to move upon the arrival of the wave front, while maintaining a similar level of reflectivity and fringe contrast, and during this stage the air gap before the LiF window closes; III: a strong wave breaks out from the sample into the window (LiF and Quartz), reducing the transparency of LiF and generating a reflective wave front in Quartz; IV: a stronger wave reaches the LiF, rendering the window opaque, and overtakes the propagating wave front in Quartz, causing the loss of fringes. V: the wave front reaches the window free surface and breaks out into the vacuum. The blue shaded region corresponds to the simulation velocity uncertainty derived with ±5% laser power, verifying the fidelity of our simulations and providing a quantitative estimate of simulation-induced uncertainty.

Ripple growth analysis

The obtained X-ray radiography image in the unit of photostimulated luminescence (PSL) is anaylzed to evaluate a growth factor of each sample[6] (Fig. S4a). The growth factor is defined, in this study, as a ratio of the areal density amplitudes between the driven (subscript D) and initial (subscript 0) ripples; $GF = \Delta\rho_{A,D}/\Delta\rho_{A,0}$, where ρ_A is the areal density and Δ means a half of the peak-to-valley amplitude. The areal density is normalized by the initial density ($Z = \rho_A/\rho_0$ in the unit of thickness) and then the growth factor equation is re-written as $GF = \Delta Z_D/\Delta Z_0$.

Given that the initial rippled foil has a constant density across the thickness, ΔZ_0 is the same as the thickness amplitude (η_0) which is measured with a white light interference profilometer. For the driven ripple, a PSL profile is extracted from a rectanglular area with a 100 pixel width and fitted with a sinusoidal function combined with a second-order-polynomial term as a background, $PSL = A_1 \sin(A_2 Y + A_3) + (A_4 + A_5 Y + A_6 Y^2)$ where A_1 is the PSL amplitude (ΔPSL), $2\pi/A_2$ is the ripple wavelength in pixels, and Y is the pixel position along the y-axis. Two independent methods, described below, are used to estimate ΔZ_D from the obtained PSL profile and determine amplitude of the driven ripple. We note that, before extracting the PSL lineout, the analyzed area is rotated to align the ripple patterns.

In the first method, the steps with known thicknesses are used to convert the PSL profile to a thickness profile. The average PSL values of the selected regions in the flat Fe foil and six Fe steps are fitted as a function of thickness (Z) with an exponential function as shown in Fig. S4b; $PSL = B_1 + B_2 \exp(-B_3 Z)$. Like an X-ray attenuation relation, the fitting coefficients of B_1, B_2, and B_3 are related to the background, incident X-ray intensity, and linear attenuation coefficient (μ, or the reciprocal of the X-ray mean free path), respectively. The PSL-Z relation is used for converting the PSL profile of the driven ripple to a thickness profile, which is fitted with the sinusoidal function combined with a second-order-polynomial term, $Z = C_1 \sin(C_2 Y + C_3) + (C_4 + C_5 Y + C_6 Y^2)$ where $C_1$is the thickness amplitude of the driven ripple (ΔZ_D). The PSL and thickness ripple lineouts are shown in Fig. S4c for both [001] and [111] Fe.

The obtained ΔZ_D is then corrected with a modulation transfer function (MTF) to account for the backlighter diagnostic spatial resolution. A partially opaque gold (Au) knife edge (KE) mounted behind a partially transparent aluminum (Al) foil is used to evaluate the MTF at the ripple wavelength (75 μm). In the selected area with a 200 pixel width (Fig. S5a), PSL values are averaged along the X-axis to extract a PSL lineout along the Y-axis (Fig. S5b). The average PSL lineout is fitted with a two-component edge-spread function, $PSL = D_1\left[\exp\left(\frac{Y-D_2}{D_3}\right)+1\right]^{-1} + D_4\left[\exp\left(\frac{Y-D_5}{D_6}\right)+1\right]^{-1} + D_7$. The fitting curve is differentiated to obtain a line spread function (LSF) and processed with a FFT (Fig. S5c). The magnitude curve of the FFT is normalized to 1 for the largest, zero-frequency value, providing a MTF curve as a function of an inverse pixel wavelength. A pixel-to-µm conversion factor is then obtained from the undriven reference ripples by comparing the wavelengths in pixel ($2\pi/A_2$) from the sinusoidal fitting of their PSL profiles with the wavelengths in µm (λ_{Ref}) from the profilometer metrology. The MTF curve as a function of the wavelength in µm is interpolated to find a MTF value at the our ripple wavelength (75 µm), MTF_{KE} (Fig. S5d). Then the growth factor (GF_1) is calculated as follwed, $GF_1 = \frac{\Delta Z_{\mathrm{D}}/MTF_{\mathrm{KE}}}{\eta_0}$.

In a second method, the reference ripple is used to covert ΔPSL_{D} to ΔZ_{D} directly. As the reference ripple is undriven, its initial amplitude ($\eta_{\mathrm{R,0}}$) from the profilometer is the same as the normalized areal density amplitude (ΔZ_{R}). The PSL amplitude (ΔPSL_{R}) is obtained from the sinusoidal fitting of its PSL profile. The slope of their linear fitting with a zero intercept ($\alpha_{\mathrm{R}} = \Delta PSL_{\mathrm{R}}/\eta_{\mathrm{R,0}}$) (Fig. S6) is used to calculate a growth factor; $GF_2 = \frac{\Delta PSL_{\mathrm{D}}/\alpha_{\mathrm{R}}}{\eta_0}$. These two GF values evaluated independently (GF_1 and GF_2) are averaged and compared with simulations.

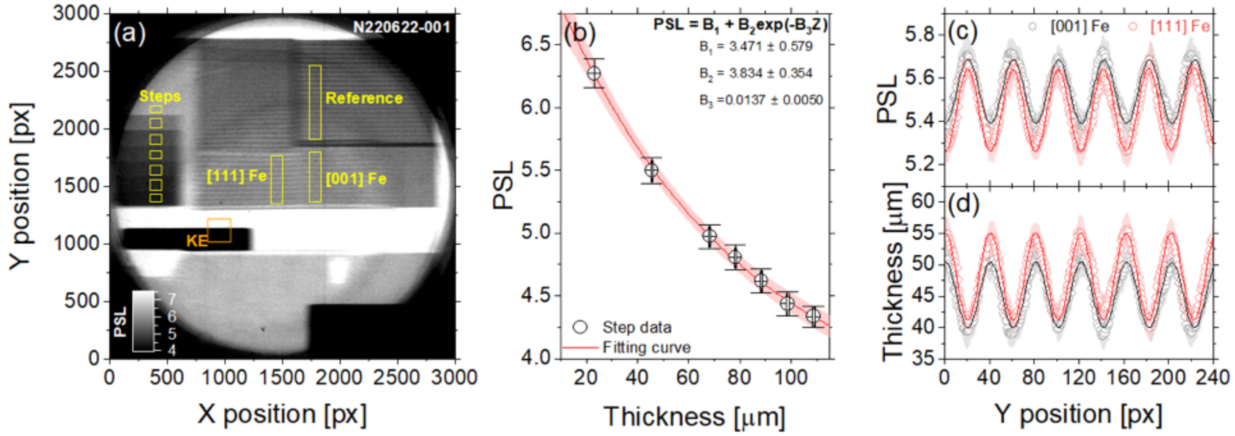

Figure S4. (a) X-ray radiography image showing regions in ripple foils, steps, and knife edge which are used for analysis. (b) PSL vs thickness data of steps are fitted with an exponential function. (c and d) PSL lineouts of three driven ripples are converted to thickness using the exponential function.

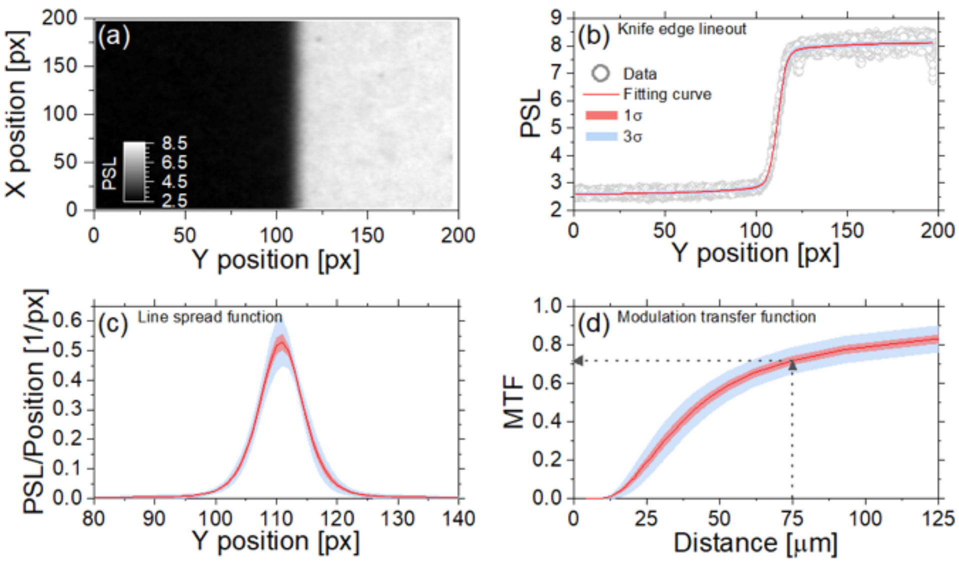

Figure S5. (a) Zoomed section of the knife edge area in the radiograph and (b) corresponding lineout in PSL units with fitted curve and shaded error. (c) Line spread function. (d) MTF as a function of distance, highlighting 75 μm as the Fe ripple wavelength.

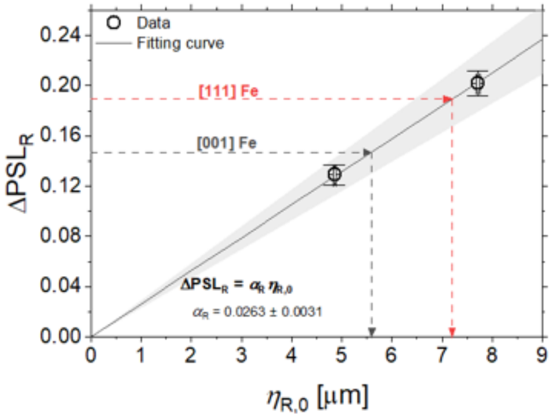

Figure S6. Conversion from amplitude in PSL to amplitude in microns using the reference ripples. Linear fit is used to convert the driven ripple amplitudes to thickness unit (indicated by dashed lines).

Random Error propagation in GF calculation

At each step of the GF calculation, random error is introduced and propagated. In the first method, utilizing the KE MTF, the GF is defined as $GF_1 = \frac{\Delta Z_{\mathrm{D}}/MTF_{\mathrm{KE}}}{\eta_0}$. The errors ($\delta$) for each term ($\Delta Z_{\mathrm{D}}$, MTF_{KE}, and η_0) are 4-7%, 3%, and 2%, respectively. The quadrature sum of these errors results in a random error of GF_1 (δGF_1) of 5-8%. In the second method, which uses the undriven reference ripples ($GF_2 = \frac{\Delta PSL_{\mathrm{D}}/\alpha_{\mathrm{R}}}{\eta_0}$), the errors are 3-5% for ΔPSL_{D}, 11% for α_{R}, and 2% for η_0. This leads to a random error of the GF_2 (δGF_2) of 11-12%. The weighted average and error of the growth factor is then calculated using the following formulas : $\bar{x} = \frac{\sum_{i=1}^{n}(x_i/\delta_i^2)}{\sum_{i=1}^{n}(1/\delta_i^2)}$ and $\delta\bar{x} = \sqrt{\frac{1}{\sum_{i=1}^{n}(1/\delta_i^2)}}$. In these equations, x_i is the data, δ_i is the error, n is the number of data. The average GF error ($\delta\overline{GF}$) ranges from 13 to 20%. Further details on the estimation of each contribution are provided below.

1. Initial ripple amplitude, η_0

The sinusoidal ripple patterns have a range of amplitudes; 1 and 1.5 µm for the driven ripples (for N220512 or N220622, respectively), and 5 and 8 µm for the reference ripples. The topography of the ripple pattern is captured using a white-light profilometer, with accuracy of 20 nm[8] (less than 2% of the amplitude). A line profile is extracted from the topography, and fitted with a sinusoidal function, resulting in a calculated amplitude (η_0) along with its associated error (less than 0.5%). The combined effects of instrumental accuracy and fitting coefficient error contribute to an initial amplitude error ($\delta\eta_0$) of 2%.

2. Scanned radiography image level, PSL

The scanned image plate exhibits a noise level which contributes to an error in the PSL value. An empirical relation for this error (δPSL) is established based on experimental data; $\delta PSL = 0.0443 \cdot PSL^{0.5}$, where δ denotes the error[9]. The PSL value for the driven ripple ranges between 4.2 and 5.8, resulting in a 2% error in the PSL measurement. According to the established relationship, the noise-to-signal ratio ($\delta\mathrm{PSL}/\mathrm{PSL}$) increases as the PSL value decreases. The highest PSL error reaches 3% for the Au KE, whose PSL value is 2.

3. PSL amplitude, ΔPSL

A ripple region of interest is rotated to align the ripple pattern and averaged transversely to extract an average PSL lineout along the pattern. The weighted average and error for the PSL lineout is then calculated using the PSL values and δPSL. The PSL lineout is fit with a sinusoidal function, combined with a 2nd-order polynomial function as a background, resulting in a PSL amplitude (ΔPSL) and its error ($\delta\Delta$PSL), which ranges from 3% to 7%, depending on the radiograph quality and ripple amplitude. The $\delta\Delta$PSL for the driven ripple area is 5% and 3% (for N220512 or N220622, respectively) and that for the reference ripple is 7%.

4. Thickness amplitude, ΔZ

Steps with a thickness (Z) error of 0.5% (from the metrology accuracy) and a PSL error of 2% (from the empirical δPSL relation) are fitted with the exponential equation, $PSL = B_1 + B_2 \exp(-B_3 Z)$. This equation can be re-arranged as a function of PSL, $Z(PSL) = \frac{1}{-B_3}\log[(PSL - B_1)/B_2]$, for converting a PSL lineout of a ripple pattern to a thickness lineout, Z.

The random error of the thickness lineout is estimated in two different ways by considering (1) the error of the PSL lineout (δPSL) using a Monte Carlo methodology with 10,000 iterations and (2) the error of the exponential fitting coefficients (B_1, B_2, and B_3). In the former, independent random sampling of the PSL value is carried out from a Gaussian distribution, $G(PSL, \delta\mathrm{PSL})$ with a mean and standard devation of PSL and δPSL, which are converted to a thickness value, $Z_{PSL}(G(PSL, \delta\mathrm{PSL}))$. The distribution of the random thicknesses is statistically analyzed to calculate a standard deviation, δZ_{PSL}. Additionally, we use a covariance matrix Σ of the exponential fitting coefficients, the Cholesky decomposition ($\Sigma = L \cdot L^T$, where L and L^T are the lower triangular matrix with positive diagonal entries and its conjugate transpose), and a random value from a uniform distribution $U(0,1)$ to generate the correlated random thicknesses ($Z_{coef,i} = \bar{Z} + U(0,1) \cdot L^T$) and their standard devation (δZ_{coef})[10]. We note that a uniform distribution is used instead of a Gaussian distribution to minimize computing instability. Their quadrature sum is used as an error in the thickness profile, $\delta Z = \left(\delta Z_{PSL}^2 + \delta Z_{coef}^2\right)^{0.5}$, which was found to be 6%. Finally, the converted thickness (Z) lineout and its associated error (δZ) is fitted with a sinusoidal function combined with a 2nd-order polynomial function, resulting in a thickness amplitude (ΔZ) and its error ($\delta\Delta$Z). The thickness error of the driven ripples is 7% for N220512 and 4% for N220622.

5. Radiography spatial resolution, *MTF*

Both PSL noise level and spatial variation are considered during the error propagation of the MTF calculation. Within the KE image, which is rotated to align the Au-Al boundary, each data point with a value of PSL_{KE} has an error of $\delta\mathrm{PSL}_{\mathrm{KE}}$. For each datapoint along a single lineout with a 1-pixel width, 2,000 independent random samples, $G(PSL_{KE}, \delta\mathrm{PSL}_{\mathrm{KE}})$ are generated following a Gaussian distribution. This process is repeated for every lineout along the X axis (i.e., parallel to the Au-Al boundary). All the generated random values are statistically analyzed at each Y position to obtain the average and standard deviation of the KE profile ($\overline{PSL_{KE}}, \delta PSL_{KE}$).

We generate 2,000 lineouts through the independent random sampling, $G(\overline{PSL_{KE}}, \delta PSL_{KE})$ for further analysis, instead of processing the initially-generated random values for minimizing computing instability. The differentiation and FFT processes to obtain the MTF are applied for every random lineout, and their average and standard deviation are calculated, resulting in a 3% error in the MTF value for 75 μm wavelengths.

6. PSL-to-thickness amplitude conversion factor, $\boldsymbol{\alpha}_{\mathbf{R}}$

The initial thickness amplitude ($\eta_{\mathrm{R,0}}$) and measured PSL amplitude (ΔPSL_{R}) for the reference ripples are linearly fitted with their respective errors, providing the conversion factor α_{R} ($\alpha_{\mathrm{R}} = \Delta PSL_{\mathrm{R}}/\eta_{\mathrm{R,0}}$). The error of the conversion factor ($\delta\alpha_{\mathrm{R}}$) is estimated through a Monte Carlo method with a covariance matrix obtained from the fitting, the Cholesky decomposition ($\Sigma = L \cdot L^T$), and an independent random sampling of $G(0,1)$[10]; $\alpha_{\mathrm{R,i}} = \overline{\alpha_{\mathrm{R}}} + G(0,1) \cdot L^T$. With 10,000 iterations, the standard deviation of the correlated random values of $\alpha_{\mathrm{R,i}}$ is estimated to 11% which corresponds to $\delta\alpha_{\mathrm{R}}$.

Hydrodynamic modeling material information

Table S1. Materials and models used in simulations. Glue layers are treated as epoxy with negligible properties

	Material	**Density (g/cm^3)**	**EOS**	**Strength model**
Common area	Be	1.858	LEOS 40	SG
	12.5% BrCH	2.0	LEOS 5128	-
	Epoxy	1.185	LEOS 5030	-
Physics layer	Fe	7.874	Multiphase[11]	SG & PTW
	LiF	2.64	LEOS 2240	SG
Witness layers	Al	2.7	LEOS 130	SG
	LiF	2.64	LEOS 2240	SG
	Ta	16.677	LEOS 730	SG
	Quartz	2.65	LEOS 2210	SG

Table S2. Parameters for Steinberg-Guinan (SG)[12] and Preston-Tonks-Wallace (PTW)[13] strength models.

SG		**PTW**	
G_0 (GPa)	77	θ	0.015
G'_P (1/GPa)	0.0226	p	3.0
G'_T (1/K)	4.55e-4	s_0	0.01
Y_0 (GPa)	0.34	s_∞	2.5e-3
$Y_{wh,max}$ (GPa)	2.5	y_0	6.625e-3
β	43	y_∞	7.5e-4
ϵ_i	0	y_1	0.03
n	0.35	y_2	0.25
		κ	0.3
		γ	1e-5
		β	0.25
		α	0.23
		T_{melt} (K)	2050
		G_0 (GPa)	87.2

Growth factor curves with various strength models

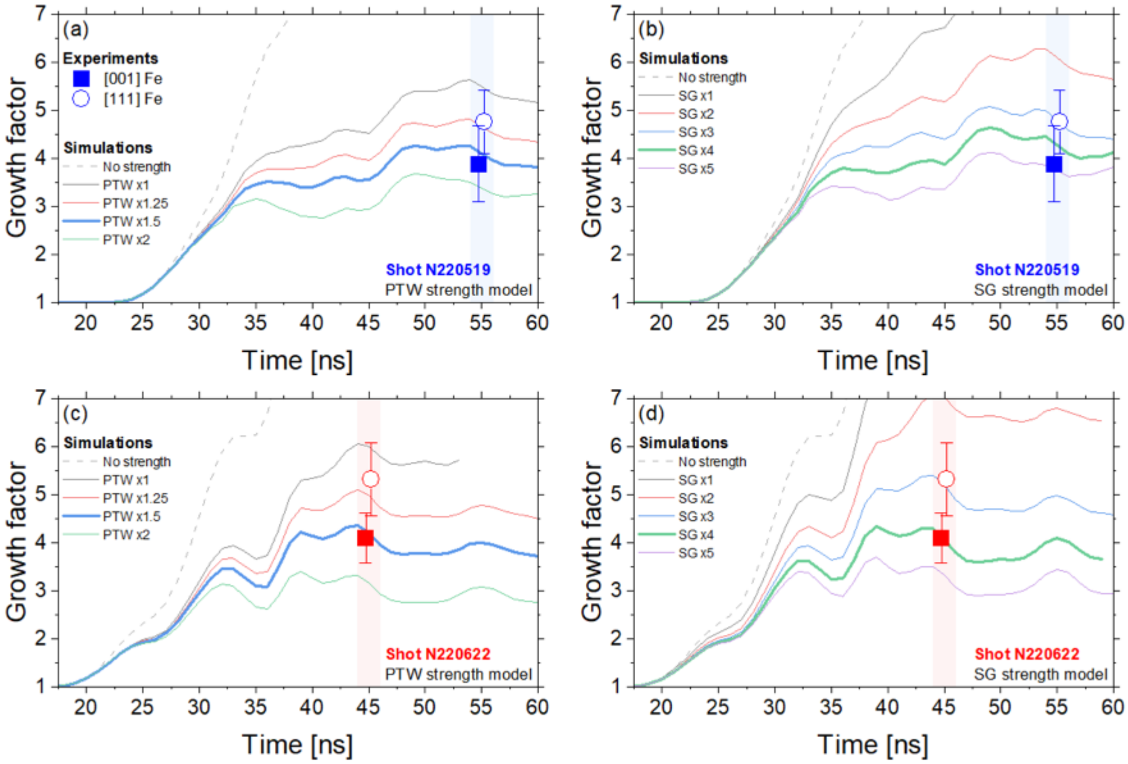

Figure S7. Growth factor curves as predicted from modeling compared to the data. Variations on the (a) PTW and (b) SG model for shot N220519 and similarly, (c-d) for shot N220622. Note that the simulation for N220622 using PTW×1 strength stops at 53 ns only due to mesh tangling causing the simulation to crash.

Compression path

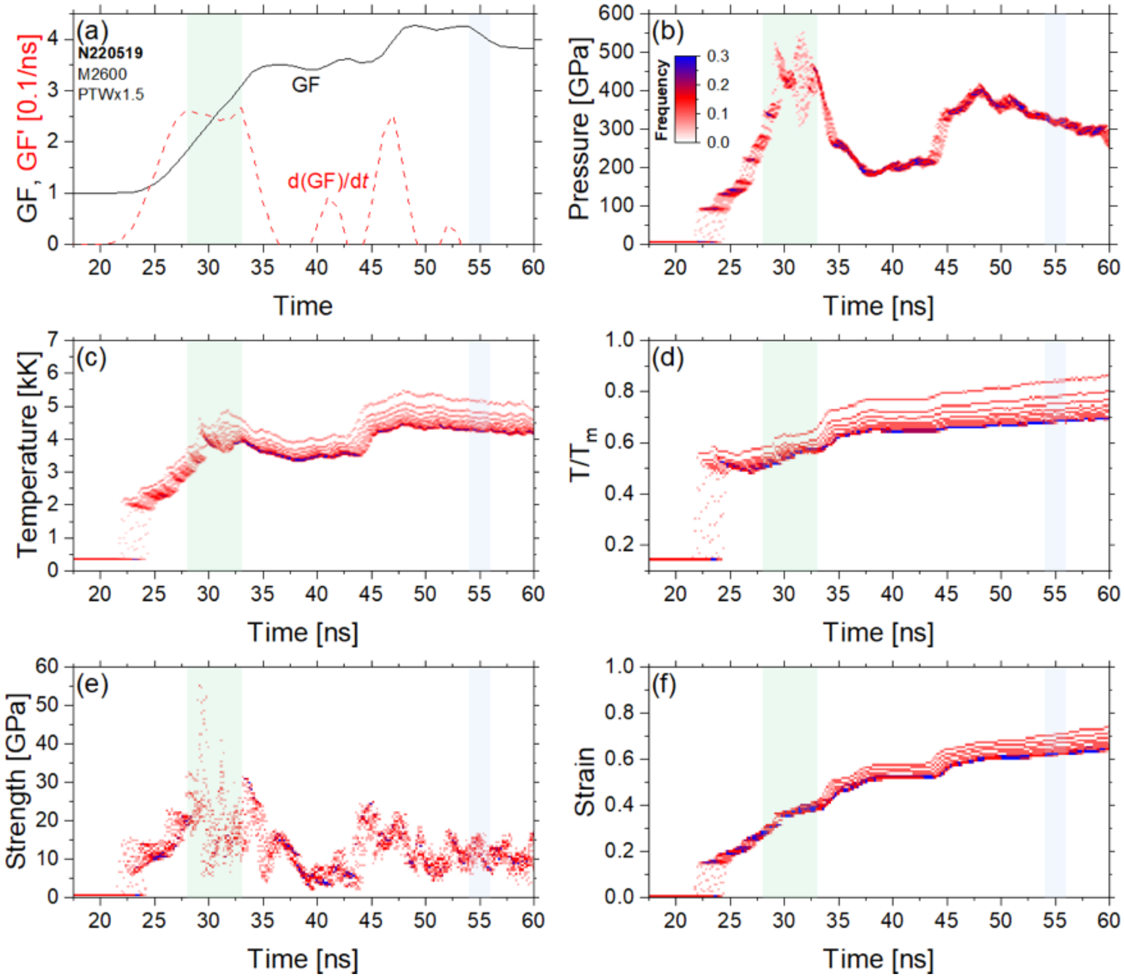

Figure S8. Different state variables take from the Ares simulation of N220519 considering the PTW×1.5 strength model. Histograms of pressure, temperature, homologous temperature, strength, and strain as functions of time show frequency of states across the iron layer in the simulation. The shaded green (28-33 ns) and blue (54-56 ns) areas depict the peak growth rate (i.e., most deformation) and backlighter timing, respectively.

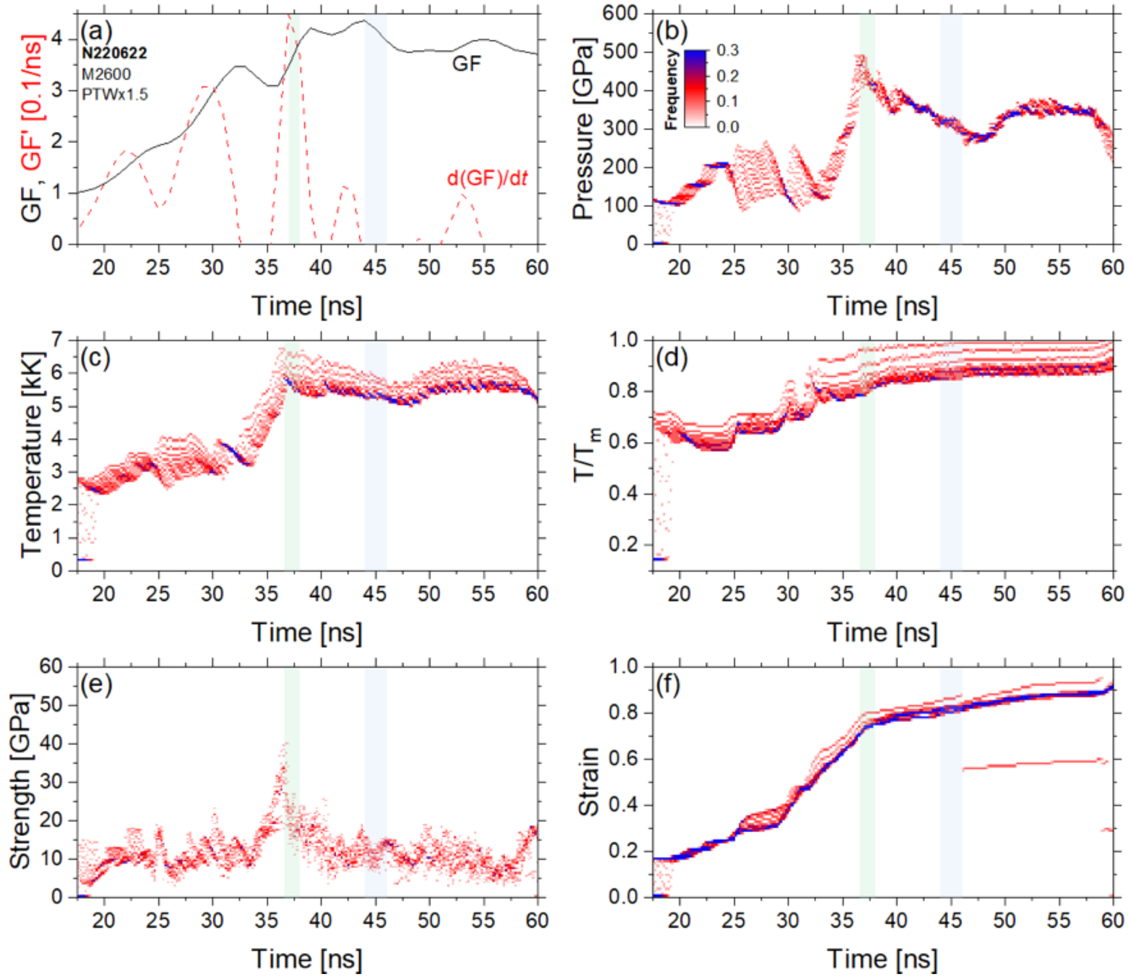

Figure S9. Different state variables take from the Ares simulation of N220622 considering the PTW×1.5 strength model. Histograms of pressure, temperature, homologous temperature, strength, and strain as functions of time show frequency of states across the iron layer in the simulation. The shaded green (37-38 ns) and blue (44-46 ns) areas depict the peak growth rate (i.e., most deformation) and backlighter timing, respectively.

Summary of GF and state variables

Table S3. Summary of growth factors, thermodynamic states (pressure and temperature), and mechanical properties (strength, strain, strain rate, and viscosity) at t_{xray} (54-56 ns for N220519 and 44-46 ns for N220622) and t_{peak} (28-33 ns for N220519 and 37-38 ns for N220622) using PTW×1.5 for e-Fe$_{[001]a}$ and ×1.25 for e-Fe$_{[111]a}$. Strength and strain correspond to von Mises stress and plastic strain, respectively. Viscosity and effective viscosity are calculated with an analytical form $[\gamma^2 + 2k^2(\mu/\rho)\gamma - Agk = 0]$ and the strength and strain rate $[\mu_{eff} = \sigma/(\sqrt{6}\dot{\varepsilon})]$, respectively.

	Time	**N220519**		**N220622**	
		ε-Fe$_{[001]\alpha}$	**ε-Fe$_{[111]\alpha}$**	**ε-Fe$_{[001]\alpha}$**	**ε-Fe$_{[111]\alpha}$**
Growth factor	t_{xray}	3.88 ± 0.79	4.75 ± 0.66	4.09 ± 0.52	5.33 ± 0.76
Pressure [GPa]	t_{peak}	403 ± 54	405 ± 54	431 ± 17	432 ± 22
Temperature [K]		3831 ± 317	3719 ± 306	5822 ± 52	5666 ± 62
Strength [GPa]		19.86 ± 4.71	17.85 ± 3.51	20.04 ± 2.57	18.56 ± 2.79
Strain		0.349 ± 0.036	0.367 ± 0.041	0.747 ± 0.007	0.808 ± 0.011
Strain rate [10^7 s^{-1}]		2.33 ± 1.86	2.67 ± 1.83	2.16 ± 0.82	3.31 ± 1.00
Pressure [GPa]	t_{xray}	321 ± 6	320 ± 6	314 ± 6	313 ± 5
Temperature [K]		4496 ± 18	4332 ± 17	5431 ± 27	5288 ± 22
Strength [GPa]		11.12 ± 1.48	9.43 ± 1.27	11.44 ± 1.29	9.14 ± 1.46
Strain		0.643 ± 0.004	0.688 ± 0.004	0.818 ± 0.004	0.886 ± 0.004
Strain rate [10^7 s^{-1}]		0.51 ± 0.21	0.54 ± 0.22	0.79 ± 0.31	0.75 ± 0.43
Viscosity [Pa·s]	-	170 ± 40	140 ± 20	130 ± 20	100 ± 20
Effective viscosity [Pa·s]	t_{peak}	350	270	380	230
	t_{xray}	890	710	590	500

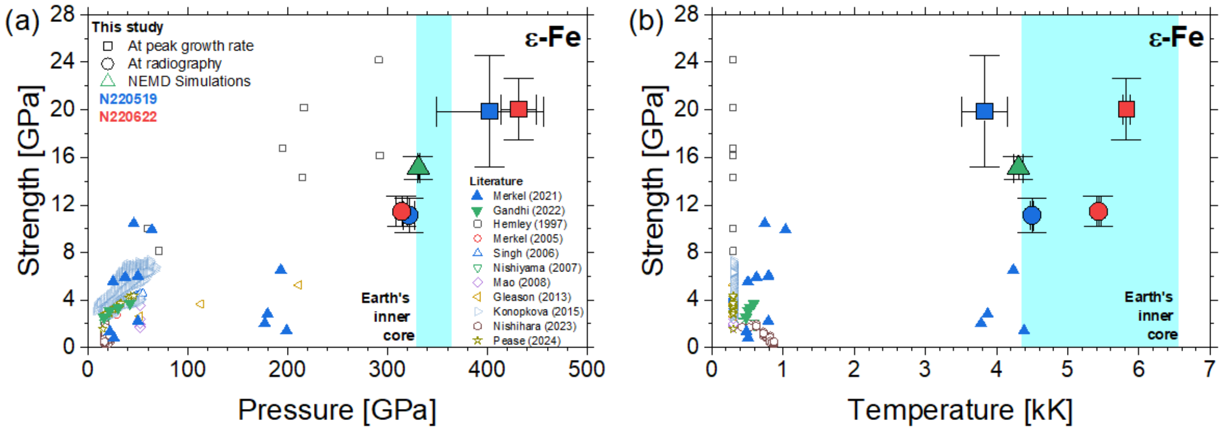

Figure S10. Strength as a function of (a) pressure and (b) temperature. Two prior laser-driven dynamic studies have reported strengths 2-5 times higher, excluded here and in Fig. 4. One multi-shock Extended X-ray Absorption Fine Structure (EXAFS) study[14] measured temperatures significantly exceeding predictions, possibly due to thermal transport from an adjacent hotter diamond window[15] rather than exceptionally high ε-Fe strength (up to 45-90 GPa at 200-560 GPa and 3500-8000 K). Another indirect laser-drive RT experiment[16] reported 40 GPa at 150 GPa, although there is higher uncertainty due to smaller ripple growth (GF of 1-2) and possibly reduced spatial resolution compared to this study.

NEMD ramp and homogeneous uniaxial-loading simulations

There are several interatomic potentials to represent Fe. For example, the Voter potential used by Kadau[17,18] is still used in recent studies[19,20], but was shown to significantly underestimate the BCC to HCP transition pressure and to lack dislocation plasticity in the BCC phase while producing a large fraction of FCC phase instead of the experimentally observed HCP phase. The Mendelev potential, widely used for studies of Fe deformation and plasticity at low pressures[21], provides a BCC-HCP transition pressure only near 60 GPa. In order to improve this situation, Gunkelmann et al[22]. presented a modified Ackland EAM potential with the appropriate phase transition pressure and a reasonable description of dislocation plasticity in the BCC phase. This potential has been successfully employed to describe shock propagation, phase transition and spall in Fe under 100 GPa[23]. It was acknowledged that the potential might not work at higher pressures, well beyond its intended applicability region. Another potential available is the EAM developed by Belonoshko and coworker[24] which fit for Fe under inner core conditions[25] but presents some problems at lower pressure and temperature[26]. Finally, there are some recent machine learning potentials[27,28] that reproduce reasonable elastic properties but have a large computational cost. In this work we have carried out the simulations of the main text with the EAM potential developed by Sun et al[29,30]. which provides a good physical description over the entire pressure-range of interest, with a relatively low computational cost.

Several MD simulation results are shown to support the discussion in the main text. The NEMD simulation results are shown in Figs. S11-S14; snapshots like the ones in Fig. 5 but for entire sample regions (Figs. S11 and S12), strength, pressure and temperature profiles (Fig. S13), and a cross-section showing the clear mirror plane of a twin (Fig. S14). We note that only 3 representative times are shown for T profiles. For shock or other non-equilibrium simulations, the temperature of certain region has to be evaluated excluding the mean velocity of that region, along each direction. For shocks, the mean velocity is zero for the directions perpendicular to the shock, but the correction is very large along the shock direction, with regions moving roughly at the piston velocity, as detailed by Righi et al[31]. The homogeneous uniaxial-loading results are shown in Figs. S15-S17; strength and pressure profiles with grain size change (Fig. S15), sample snapshots (Fig. S16), and a cross-section (Fig. S17). [111] grains are clearly smaller and have lower strength at the relevant times, during the hold stage of the loading. The overall microstructure is the same as for NEMD loading. Both MD simulation results are summarized in Table S4.

The role of GB plasticity under shocks is complex. Initial studies in FCC metals showed GB hardening[32]. In the Hall-Petch regime dislocation plasticity dominates, and strength increases as grain size decreases. On the other hand, when GB plasticity dominates, in the inverse Hall-Petch regime, strength increases with grain size[33], and this would be the regime for both Fe samples. Some details on GB plasticity in our homogeneous uniaxial-loading simulation are shown in Fig. S18. For the PTM analyzer in Fig. S18(a), GB atoms include both BCC (blue) and "Other (gray)" structure types. Most of the BCC atoms disappear if using a more stringent phase identification criteria, by reducing the RMSD parameter. In Fig. S18(b), the largest displacements are associated with GBs in the top and bottom regions of the selected view, with some large displacements inside the middle grain, due to formation of twins and stacking faults. Fig. S18(c) shows a quantitative measurement of GB activity, the cumulative GB shear strain, that has been used as proxy for GB plasticity[34]. This cumulative shear provides clear evidence of larger GB contributions to deformation of [111] samples.

We have carried out additional homogeneous uniaxial-loading simulations using linear strain and temperature ramp at 10^7 /s, to check on a possible increase of dislocation activity at lower strain-rates, similar to the experimental values. We find similar microstructures, but larger dislocation densities, supporting the use of models like PTW, which are based on dislocation plasticity. However, we emphasize that dislocation detection with DXA within OVITO[35] is challenging for core conditions which involve high stress and temperature with large nanoscale gradients.

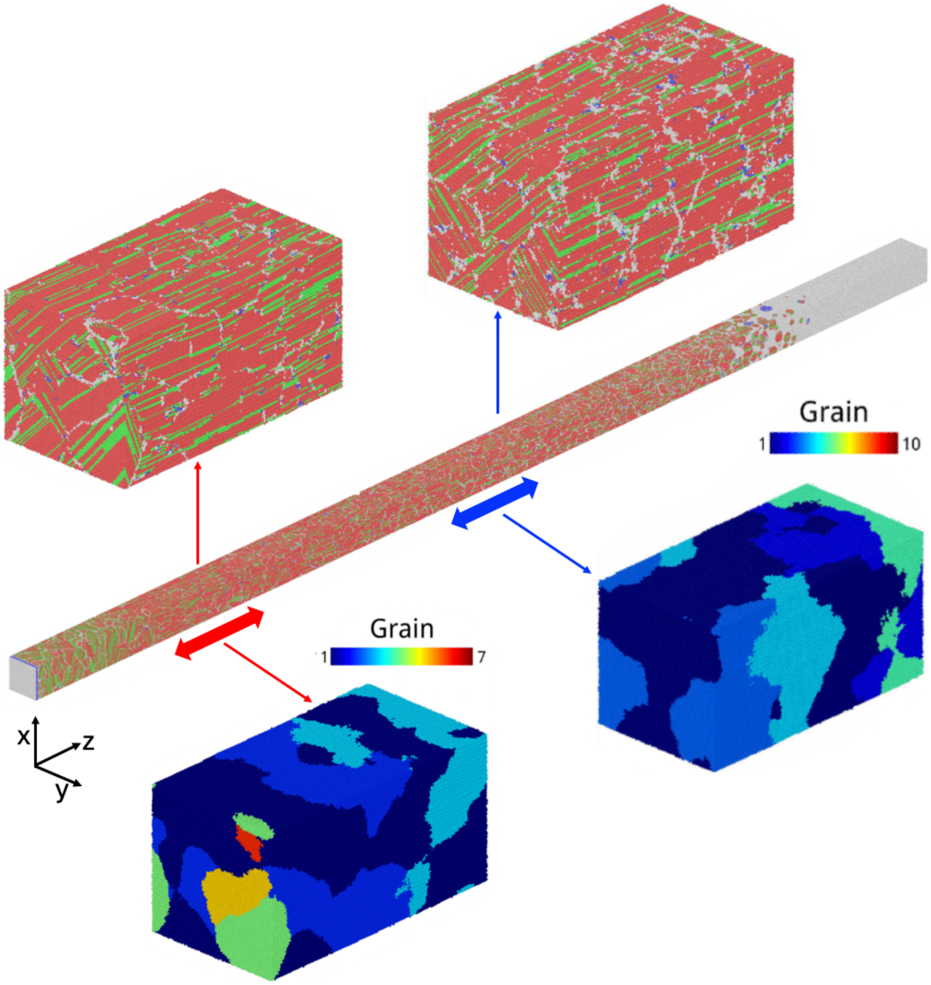

Figure S11. Snapshot of Fe samples with [001] orientation at 170 ps from the NEMD ramp-compression simulations, with zoomed-in snapshots of (top insets) microstructure and (bottom insets) grain identification. Atoms are colored by their structures: blue for BCC, red for HCP, green for FCC, and gray for others. Note that the lateral sizes of the samples and insets are 20 nm.

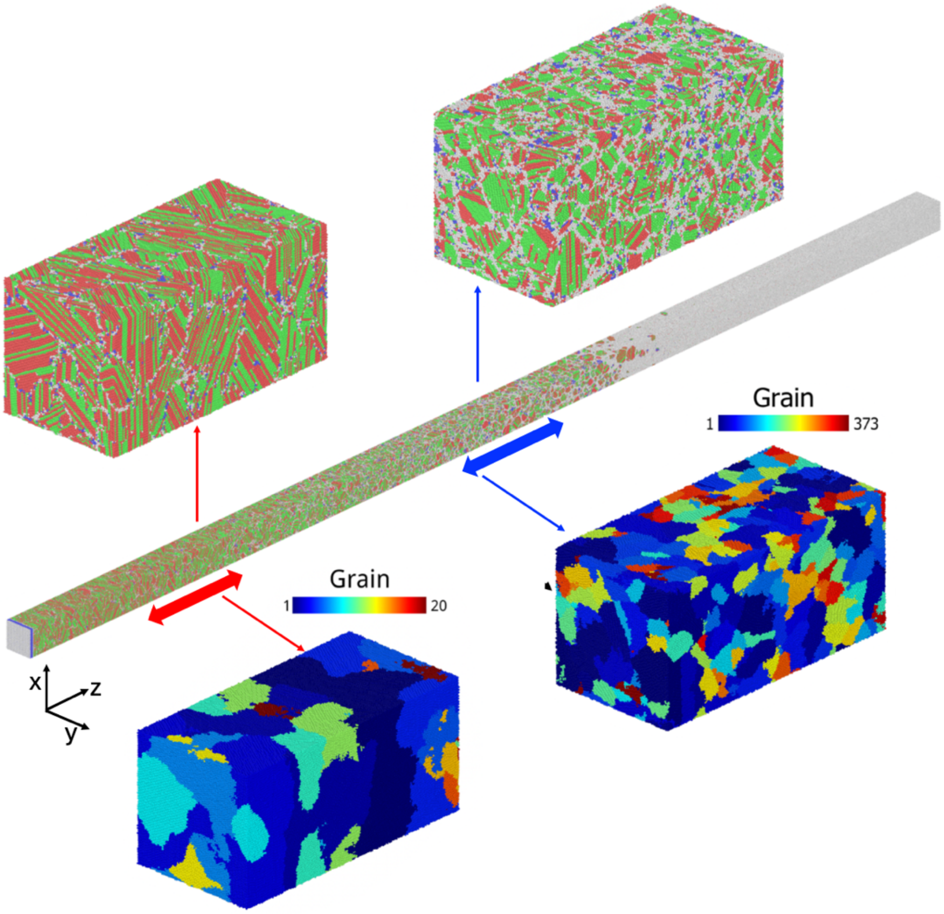

Figure S12. Snapshot of Fe samples with [111] orientation at 175 ps from the NEMD ramp-compression simulations, with zoomed-in snapshots of (top insets) microstructure and (bottom insets) grain identification. Atoms are colored by their structures: blue for BCC, red for HCP, green for FCC, and gray for others. Note that the lateral sizes of the samples and insets are 20 nm.

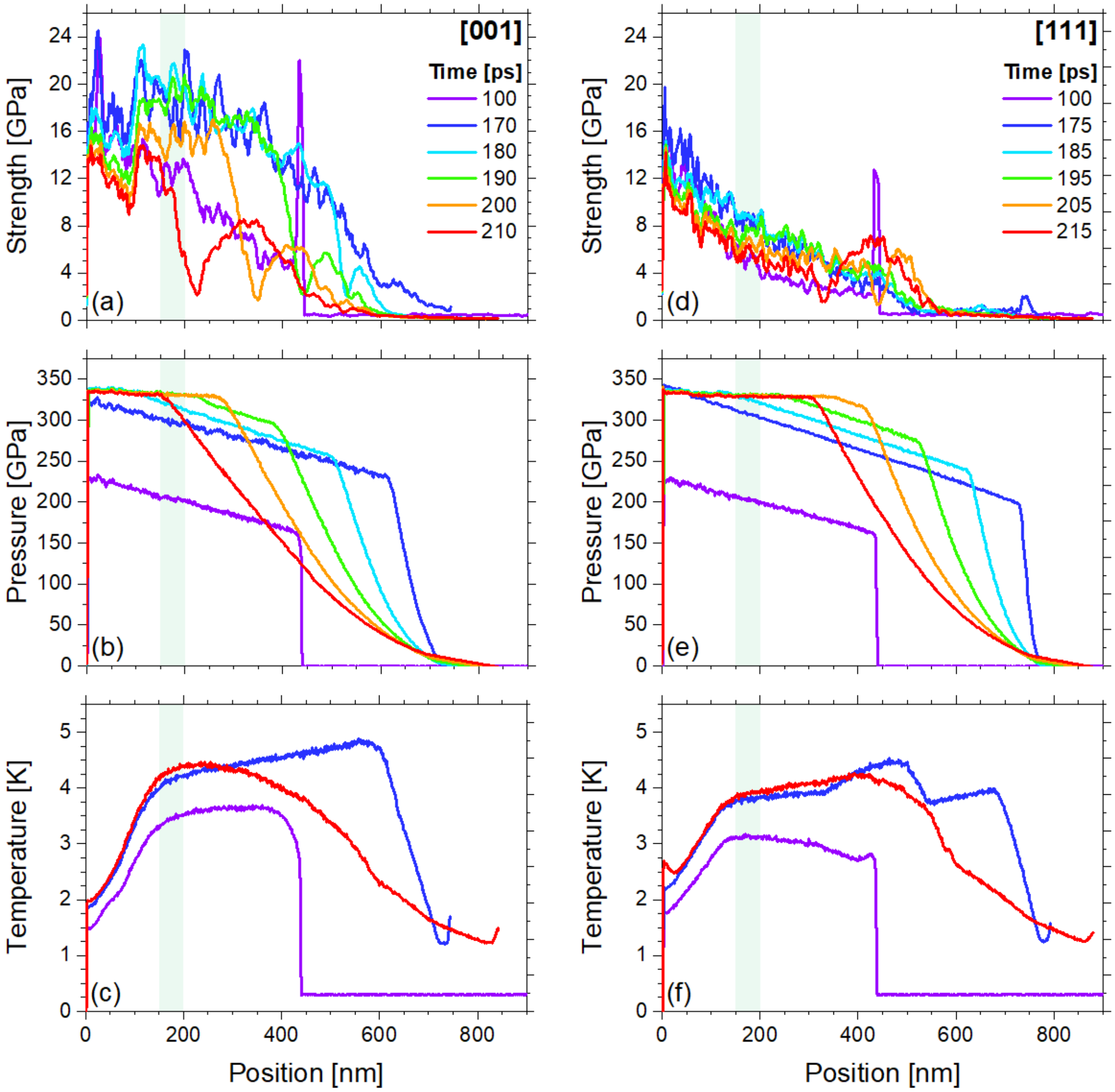

Figure S13. Profiles of strength (von Mises stress), pressure, and temperature from the NEMD ramp-compression simulations; (a-c) for the [001] sample at 100-210 ps, and (d, e, f) for the [111] sample at 100-215 ps. Position denotes the distance from the piston along the compression axis. Green shading (150-200 nm) marks the regions over which data are averaged to obtain representative values. The times differ slightly between orientations due to the differences in their elastic wave velocities. The compression wave reaches the free surface at <170-175 ps, generating a returning rarefaction wave that produces a gradual decrease in strength, pressure, and temperature toward the free surface during the later stage (170-215 ps). The piston, located at 0 nm, is maintained at 0 K, acting as a heat sink and causing a temperature decrease within the 0-150 nm region adjacent to it. Only 3 representative times are shown for temperature profiles. During ramping up to 330 GPa, strength remains 18-20 GPa for ε-Fe$_{[001]\alpha}$ 8-9 GPa for ε-Fe$_{[001]\alpha}$ but eventually decreases to 15 GPa and 6 GPa, when plasticity has fully evolved and reached a steady state.

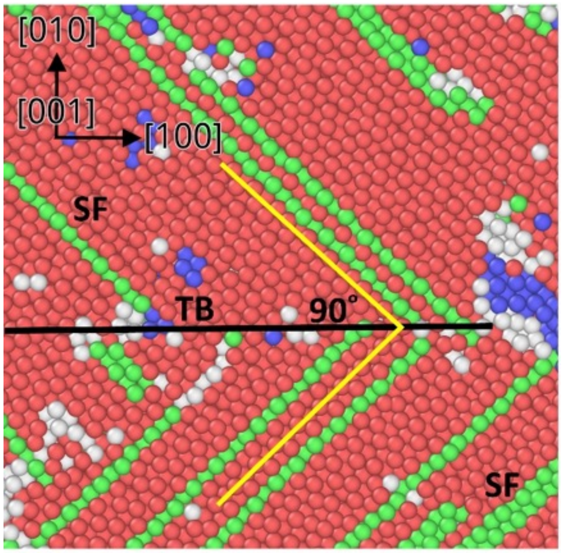

Figure S14. Cross-section of the [001] Fe sample at 170 ps from the NEMD ramp-compression simulation, ~200 nm ahead of the piston, showing stacking faults (SF, green atomic planes) and twin boundary (TB, black line). Atoms are colored by their structures: blue for BCC, red for HCP, green for FCC, and gray for others. Yellow lines indicate a 90° degree angle.

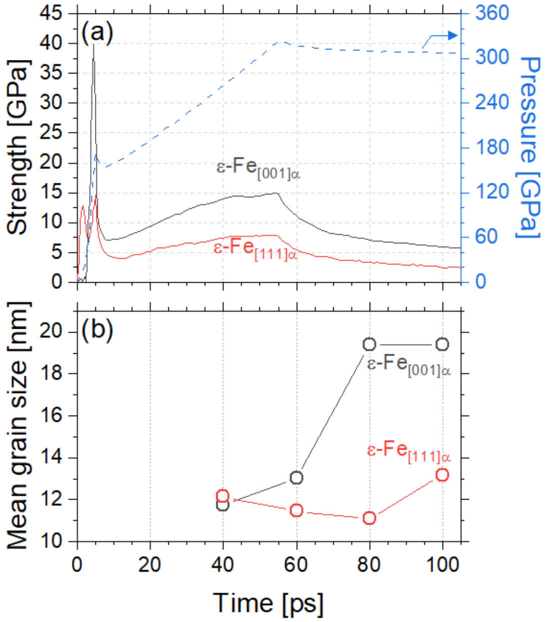

Figure S15. (a) Strength (von Mises stress) and pressure and (b) mean grain size as a function of time from the homogeneous uniaxial-loading simulations of Fe samples with [001] and [111] orientations.

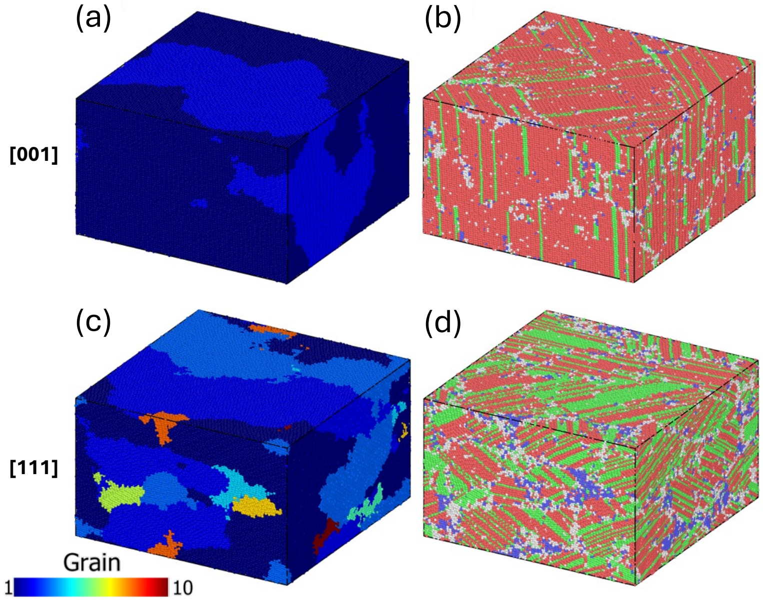

Figure S16. Snapshot of Fe samples with (a, b) [001] and (c, d) [111] orientations at the end of the homogeneous uniaxial-loading simulations (40% strain and 105 ps). Atoms are colored by (a, c) their grain identifiers with grains ranked by size (grain 1 being the largest), and (b and d) their structures according to PTM: blue for BCC, red for HCP, green for FCC, and gray for others.

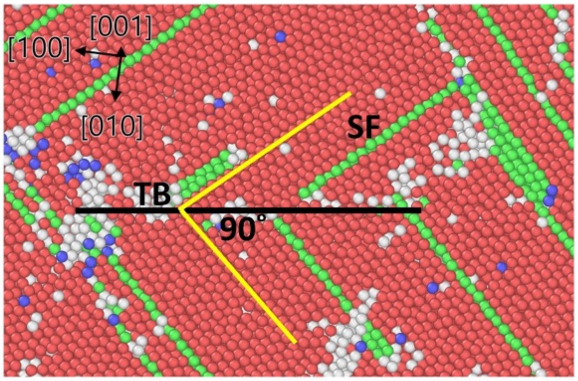

Figure S17. Cross-section of the [001] Fe sample at 105 ps from the homogeneous uniaxial-loading simulation, showing stacking faults (SF, green atomic planes) and twin boundary (TB, black line). Atoms are colored by their structures: blue for BCC, red for HCP, green for FCC, and gray for others. Yellow lines indicate a 90° angle.

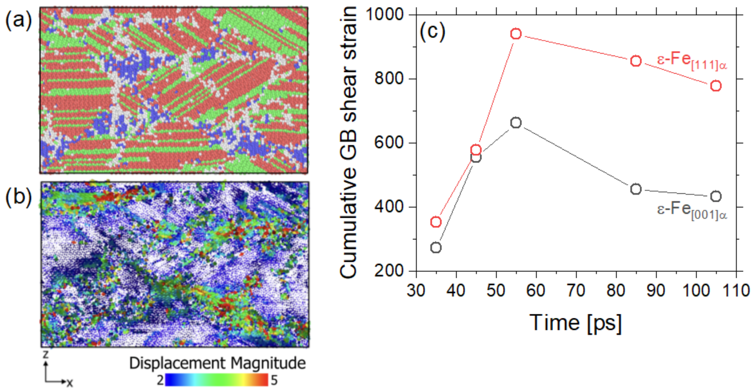

Figure S18. Cross-section of the [111] Fe sample at 105 ps from the uniaxial-loading simulation. Atoms are colored by (a) their structures according to PTM (blue for BCC, red for HCP, green for FCC, and gray for others) and (b) their displacement magnitude (x0.1 nm). Deformation is concentrated at gain boundaries (gray) rather than within grain interiors (blue, red, or green). (c) Cumulative shear strain for grain-boundary (GB) atoms as function of time. The higher GB strain in the [111] sample can be explained by enhanced GB sliding associated with a larger number of smaller grains.

Table S4. Summary of the MD simulation results. The NEMD shock results are spatially-averaged over a region of 150-200 nm ahead of the piston at 200-205 ps, while the homogeneous uniaxial-loading results are averaged temporally over the last 10 ps (95-105 ps) across the simulation cell. The strength (von Mises stress) values from the uniaxial-loading simulations are systematically lower than both experimental and NEMD results, possibly attributable to the absence of stress gradients or wave fronts in the controlled loading geometry. Temperatures indicate the temperature at the time of the strength measurement, in the region indicated. Higher temperatures for homogeneous loading would contribute to the observed lower strength.

	NEMD shock (150-200 nm)		**Homogeneous uniaxial-loading**	
	ε-Fe$_{[001]\alpha}$	**ε-Fe$_{[111]\alpha}$**	**ε-Fe$_{[001]\alpha}$**	**ε-Fe$_{[111]\alpha}$**
Time [ps]	210	215	95-105	
Pressure [GPa]	331 ± 1	330 ± 1	307.8 ± 0.2	
Temperature [K]	4305 ± 65	3897 ± 33	5000	
Strength [GPa]	15.12 ± 0.95	6.25 ± 0.49	5.97 ± 0.16	2.57 ± 0.11

Viscosity of Fe

The viscosity of Fe reported in the literature spans a wide range from 10^{-4}-10^{-2} Pa·s for liquid Fe to 10^{14}-10^{18} Pa·s for ε-Fe under inner core conditions. The liquid Fe viscosities, measured using falling-sphere method[36–38] and supported by *ab initio* molecular dynamics (MD) simulations[39], establish a lower bound for comparison. Our results (10^2 Pa·s) therefore correspond to solid-phase measurements. The highest inner-core estimates (10^{16}-10^{18} Pa·s) are derived from the dislocation creep models based on density functional theory (DFT) calculations. Machine learning-based MD simulations suggest that high vacancy concentrations can lower these by a factor of 10^2 (to 10^{14}-10^{16} Pa·s), with further reduction possible via grain boundary sliding[40]. These ranges are consistent with Earth's nutation modeling (2×10^{14}-7×10^{14} Pa·s)[41], a static compression extrapolations (10^{15}-10^{18} Pa·s)[42], and a maximum estimate (4×10^{15} Pa·s) using a minimum strain for texture development (0.5), a maximum inner core age (1100 Ma) and a minimum stress condition (0.12 Pa)[43].

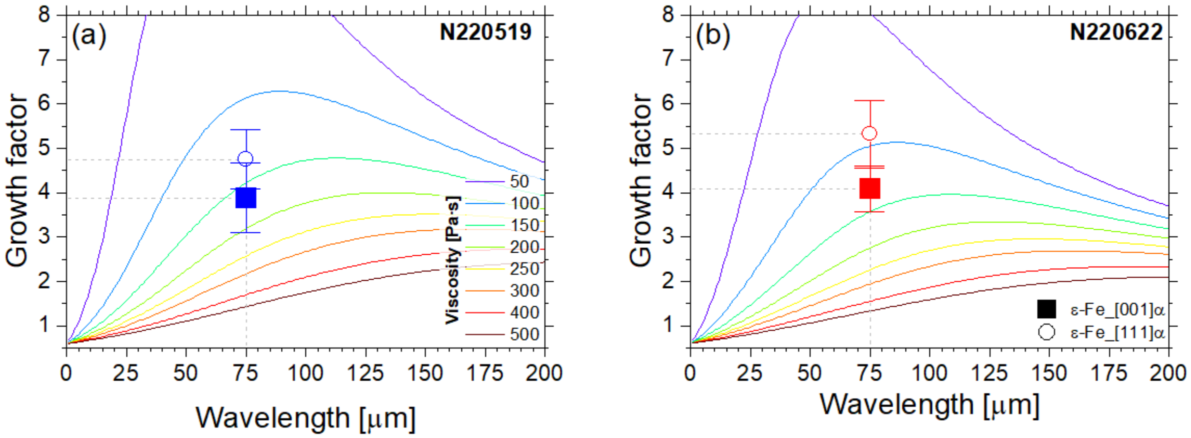

Figure S19. Analytic RT dispersion curves for (a) N220519 and (b) N220622 with varying viscosity. The symbol corresponds to the experimental measurements.

References

1. MacFarlane, J. J. VISRAD—A 3-D view factor code and design tool for high-energy density physics experiments. *Journal of Quantitative Spectroscopy and Radiative Transfer* **81**, 287–300 (2003).
2. Celliers, P. M. *et al.* Insulator-to-Conducting Transition in Dense Fluid Helium. *Physical Review Letters* **104**, 184503 (2010).
3. Celliers, P. M. & Millot, M. Imaging velocity interferometer system for any reflector (VISAR) diagnostics for high energy density sciences. *Review of Scientific Instruments* **94**, 011101 (2023).
4. Kirsch, L. E. *et al.* Refractive index of lithium fluoride to 900 gigapascal and implications for dynamic equation of state measurements. *Journal of Applied Physics* **125**, 175901 (2019).
5. Jensen, B. J., Holtkamp, D. B., Rigg, P. A. & Dolan, D. H. Accuracy limits and window corrections for photon Doppler velocimetry. *Journal of Applied Physics* **101**, 013523 (2007).
6. Kim, Y.-J. *et al.* Effect of compression path on Rayleigh-Taylor instability growth of solid copper. *AIP Conference Proceedings* **2844**, 370002 (2023).
7. Bevington, P. R. & Robinson, D. K. *Data Reduction and Error Analysis for the Physical Sciences*. (McGraw-Hill, Boston, Mass., 2003).
8. Krygier, A. *et al.* Extreme Hardening of Pb at High Pressure and Strain Rate. *Physical Review Letters* **123**, 205701 (2019).
9. Maddox, B. R. *et al.* High-energy x-ray backlighter spectrum measurements using calibrated image plates. *Review of Scientific Instruments* **82**, 023111 (2011).
10. Kim, Y.-J. *et al.* Evidence for Dissociation and Ionization in Shock Compressed Nitrogen to 800 GPa. *Physical Review Letters* **129**, 015701 (2022).

11. Wu, C. J. *et al.* Wide-ranged multiphase equation of state for iron and model variations addressing uncertainties in high-pressure melting. *Physical Review B* **108**, 014102 (2023).
12. Steinberg, D. J. Equation of State and Strength Properties of Selected Materials. (1996).
13. Belof, J. L. *et al.* Rayleigh-Taylor strength experiments of the pressure-induced α→ε→α′ phase transition in iron. *AIP Conference Proceedings* **1426**, 1521–1524 (2012).
14. Ping, Y. *et al.* Solid Iron Compressed Up to 560 GPa. *Physical Review Letters* **111**, 065501 (2013).
15. Sio, H. *et al.* Extended X-ray absorption fine structure of dynamically-compressed copper up to 1 terapascal. *Nat Commun* **14**, 7046 (2023).
16. Huntington, C. M. *et al.* Investigating iron material strength up to 1 Mbar using Rayleigh-Taylor growth measurements. *AIP Conference Proceedings* **1793**, 110007 (2017).
17. Kadau, K., Germann, T. C., Lomdahl, P. S. & Holian, B. L. Microscopic View of Structural Phase Transitions Induced by Shock Waves. *Science* **296**, 1681–1684 (2002).
18. Kadau, K., Germann, T. C., Lomdahl, P. S. & Holian, B. L. Atomistic simulations of shock-induced transformations and their orientation dependence in bcc Fe single crystals. *Physical Review B* **72**, 064120 (2005).
19. Shao, J.-L., He, W., Xi, T. & Xin, J. Microscopic insight into the structural transition of single crystal iron under the ramp wave loading. *Computational Materials Science* **182**, 109772 (2020).
20. Yu, J., Shao, J., Shu, H., Huang, X. & Fu, S. Microstructural and mechanical analysis on the shock-induced spalling with structural transformation in single crystal iron: Atomistic simulations. *Materials Today Communications* **39**, 109291 (2024).

21. Mendelev, M. I. *et al.* Development of new interatomic potentials appropriate for crystalline and liquid iron. *Philosophical Magazine* **83**, 3977–3994 (2003).
22. Gunkelmann, N. *et al.* Polycrystalline iron under compression: Plasticity and phase transitions. *Physical Review B* **86**, 144111 (2012).
23. Righi, G. *et al.* A spall and diffraction study of nanosecond pressure release across the iron ε-α phase boundary. *Acta Materialia* **257**, 119148 (2023).
24. Belonoshko, A. B., Ahuja, R. & Johansson, B. Quasi– *Ab Initio* Molecular Dynamic Study of Fe Melting. *Physical Review Letters* **84**, 3638–3641 (2000).
25. Belonoshko, A. B. *et al.* Origin of the Low Rigidity of the Earth's Inner Core. *Science* **316**, 1603–1605 (2007).
26. Deluigi, O. R. & Bringa, E. M. Mechanical properties of hcp Fe at high pressures and temperatures from large-scale molecular dynamics simulations. *Journal of Applied Physics* **136**, 195901 (2024).
27. Li, Z. & Scandolo, S. Deep-learning interatomic potential for iron at extreme conditions. *Physical Review B* **109**, 184108 (2024).
28. Nikolov, S. *et al.* Probing iron in Earth's core with molecular-spin dynamics. *Proceedings of the National Academy of Sciences* **121**, e2408897121 (2024).
29. Sun, Y. *et al. Ab Initio* Melting Temperatures of Bcc and Hcp Iron Under the Earth's Inner Core Condition. *Geophysical Research Letters* **50**, e2022GL102447 (2023).
30. Sun, Y. *et al.* Unveiling the effect of Ni on the formation and structure of Earth's inner core. *Proceedings of the National Academy of Sciences* **121**, e2316477121 (2024).
31. Righi, G. *et al.* Towards the ultimate strength of iron: spalling through laser shock. *Acta Materialia* **215**, 117072 (2021).

32. Bringa, E. M. *et al.* Ultrahigh Strength in Nanocrystalline Materials Under Shock Loading. *Science* **309**, 1838–1841 (2005).
33. Li, W. *et al.* Unraveling the Hall-Petch to inverse Hall-Petch transition in nanocrystalline high entropy alloys under shock loading. *International Journal of Plasticity* **178**, 104010 (2024).
34. Deluigi, O. *et al.* Influence of Grain Size on Mechanical Properties of a Refractory High Entropy Alloy under Uniaxial Tension. *Crystals* **13**, 357 (2023).
35. Stukowski, A. & Albe, K. Dislocation detection algorithm for atomistic simulations. *Modelling and Simulation in Materials Science and Engineering* **18**, 025016 (2010).
36. Rutter, M. D. *et al.* Viscosity of liquid Fe at high pressure. *Physical Review B* **66**, 060102 (2002).
37. Terasaki, H. *et al.* Viscosity change and structural transition of Molten Fe at 5 GPa. *Geophysical Research Letters* **29**, 68 (2002).
38. Kono, Y. *et al.* High-pressure viscosity of liquid Fe and FeS revisited by falling sphere viscometry using ultrafast X-ray imaging. *Physics of the Earth and Planetary Interiors* **241**, 57–64 (2015).
39. Li, Q., Sun, T., Zhang, Y., Xian, J.-W. & Vočadlo, L. Atomic transport properties of liquid iron at conditions of planetary cores. *The Journal of Chemical Physics* **155**, 194505 (2021).
40. Li, Z. & Scandolo, S. Elasticity and Viscosity of hcp Iron at Earth's Inner Core Conditions From Machine Learning-Based Large-Scale Atomistic Simulations. *Geophysical Research Letters* **49**, e2022GL101161 (2022).
41. Koot, L. & Dumberry, M. Viscosity of the Earth's inner core: Constraints from nutation observations. *Earth and Planetary Science Letters* **308**, 343–349 (2011).

42. Gleason, A. E. & Mao, W. L. Strength of iron at core pressures and evidence for a weak Earth's inner core. *Nature Geoscience* **6**, 571–574 (2013).
43. Park, Y. *et al.* Viscosity of Earth's inner core constrained by Fe–Ni interdiffusion in Fe–Si alloy in an internal-resistive-heated diamond anvil cell. *American Mineralogist* **108**, 1064–1071 (2023).